Tuning of structure and host dynamics via yttrium doping in Bi_2O_3 to enhance oxygen ion diffusion

Prabhatasree Goel,[1,*] Mayanak K. Gupta,[1,2] Sajan Kumar,[1,2] Ranjan Mittal,[1,2,†] Aditya Prasad Roy,[3] Dipanshu Bansal,[3] Manh Duc Le,[4] Rakesh Shukla,[2,5] Srungarpu N. Achary,[2,5] Sanghamitra Mukhopadhyay,[4] Avesh K. Tyagi,[2,5] and Samrath L. Chaplot[1,2]

[1]*Solid State Physics Division, Bhabha Atomic Research Centre, Trombay, Mumbai 400085, India*
[2]*Homi Bhabha National Institute, Anushaktinagar, Mumbai 400094, India*
[3]*Department of Mechanical Engineering, Indian Institute of Technology Bombay, Mumbai, MH 400076, India*
[4]*ISIS Neutron and Muon Source, Rutherford Appleton Laboratory, Didcot, Oxon OX11 0QX, United Kingdom*
[5]*Chemistry Division, Bhabha Atomic Research Centre, Trombay, Mumbai 400085, India*

(Received 5 June 2023; accepted 7 September 2023; published 25 September 2023)

We present a comprehensive study of the structure and dynamics of Bi_2O_3 with different Y-doping concentrations [$(Bi_{1-x}Y_x)_2O_3$ ($x = 0$, 0.2, and 0.4)] using inelastic neutron scattering (INS) and Raman scattering experiments supplemented by *ab initio* molecular dynamics (AIMD) and lattice dynamics simulations. Our INS and Raman experiments show a significant change in the vibrational spectrum between normal α-Bi_2O_3 and superionic δ-Bi_2O_3, and a pronounced change with temperature in Y-doped compounds, which reveal the presence of soft anharmonic phonons and the role of host dynamics in fast oxygen diffusion. The results corroborate very well the AIMD simulations. Further, the AIMD simulations show a faster oxygen diffusion with 20% Y-doping than with 40%. Our analysis reveals that the Bi_4O tetrahedral volume distribution plays a crucial role in O diffusion; a larger mean volume of Bi_4O leads to faster oxygen diffusion.

DOI: 10.1103/PhysRevMaterials.7.095402

I. INTRODUCTION

Oxide ion conduction is a desirable trait in materials for their use in various applications, such as fuel cells, gas sensors, and ceramic oxygen generators, and it is avidly studied by researchers to understand their basic physics. Like many other Li-, Na-, and Cu-based superionic compounds, high ionic conductivity in these compounds is primarily attributed to many vacant sites at high temperatures [1–20]. Yttria-stabilized zirconia (YSZ), a widely used oxygen-ion conductor, is a typical example. In this category, bismuth sesquioxide (Bi_2O_3) leads, as ZrO_2-based electrolytes [21], exhibit low oxide ion conductivity below 800 K and also require very high sintering temperatures to the tune of 2000 K. However, the ionic conductivity of Bi_2O_3 is about two orders greater than the YSZ at above ∼1000 K (of the order of $\sim 1\,S\,cm^{-1}$) [22]. Several studies on Bi_2O_3 have shown that the superionic Bi_2O_3 phase can be stabilized [23] at a much lower temperature by suitable rare-earth (R) element substitution $(Bi_{1-x}R_x)_2O_3$ (R = Nd, Sm, Gd, Dy, Y) [24–27]. Hence, it is a potential superionic material for application near ambient conditions. To further improve the material property and design of such superionic materials for lower temperature applications, it is required to understand the role of crystal structure, host dynamics, and rare-earth substitutions on O-diffusion at the microscopic level.

Bi_2O_3 occurs in the monoclinic phase at ambient conditions referred to as α-phase. Its crystal structure shows a $P2_1/c$ space group consisting of layers of bismuth (along the a-axis) separated by oxygen layers. Raman and infrared studies have been carried out on α-Bi_2O_3 [28–32]. It is reported that the Raman spectra extended up to $445\,cm^{-1}$ and the bands below $200\,cm^{-1}$ are very sharp [31]. As the phase changed to disordered cubic δ-phase, a decrease in the number of Raman modes was seen [32]. At 1003 K, Bi_2O_3 transforms to a superionic cubic phase referred to as δ-phase, a highly anion disordered cubic fluorite-type phase (space group Fm-$3m$) in which 25% of oxygen sites are vacant. The presence of 25% vacancies and the high polarizability of the cation network due to the $6s^2$ lone pair electrons on Bi^{3+} are said to be the reasons for high ion mobility in the δ-Bi_2O_3 phase [33,34]. The crystal structures of the ambient condition phase, α-Bi_2O_3, and the high-temperature phase, δ-Bi_2O_3, are shown in Fig. S1 of the Supplemental Material [35]. Several studies [36–38] have been carried out to investigate the formation and ionic conduction properties of the various polymorphs of Bi_2O_3.

The δ-Bi_2O_3 phase exists above 1003 K [1,38] up to 1093 K, the melting temperature of the compound [1,39]. The disordered cubic structure, δ-Bi_2O_3 is essential for the emergence of macroscopic diffusion in Bi_2O_3, which has potential technological applications. The δ-phase can be stabilized at lower temperatures by doping various types of ions, including rare-earth elements [2,22,32,33,40–43]. Optimum concentration of dopant is desired to stabilize the δ-phase at ambient temperature. There are recent studies on oxide ion conductors that underline the importance of dopants

*knp@barc.gov.in
†rmittal@barc.gov.in

for adopting flexible/variable coordination and geometrical arrangement around a cation to create vacancies and disorder in the Bi-O sublattice, thereby enhancing conductivity [44,45]. These stabilized oxides exhibit fast ion diffusion at relatively lower temperatures of approximately 600–700 K. Although the absolute values of conductivity in the doped compounds at 600–700 K are less than that in the pure δ-cubic phase at above 1000 K, there is macroscopic diffusion at lower temperatures that could be utilized successfully technologically [46–49].

Earlier neutron scattering studies on Bi_2O_3 mainly focused on the undoped compound [2,13,28,29,31,32,50]. In this work, we have focused on the Y-doped compounds to understand the macroscopic diffusion of oxygen ions in terms of their basic microscopic structural and dynamical features. Y doping can affect the O dynamics primarily in two ways: (a) it stabilizes the superionic δ-phase, which provides many vacant sites and helps in oxygen migration, and (b) it alters the host dynamics. There have been reports [30,51] on different Y-doping levels for an appreciable diffusion at lower temperatures. Our interest here is to see if we can find a convincing correlation between the doping level and fast oxide ion conduction. Hence, we have carried out detailed vibrational studies on the undoped, 20% Y-doped, and 40% Y-doped Bi_2O_3 using INS and Raman scattering experiments supported by AIMD simulations. These insightful atomistic studies of ionic mobility help to elucidate the importance of host and dopant dynamics in the oxygen conduction mechanism in these oxides. The results are useful to understand the role of Y-doping in lowering the fast ion conduction temperature, which in turn improves the usability of these oxides. This would facilitate improved efforts in the smart design and tuning of these useful solid ionic conductors.

II. EXPERIMENTAL AND COMPUTATIONAL DETAILS

$(Bi_{0.8}Y_{0.2})_2O_3$ and $(Bi_{0.6}Y_{0.4})_2O_3$ samples were prepared by solid-state reaction of Bi_2O_3 and Y_2O_3. Prior to their use for the reaction, Bi_2O_3 was heated at 673 K for 6 h and Y_2O_3 was heated at 1073 K for 12 h. The homogeneous mixtures of appropriate amounts of Bi_2O_3 and Y_2O_3 for composition, $(Bi_{0.8}Y_{0.2})_2O_3$, and $(Bi_{0.6}Y_{0.4})_2O_3$ were pressed into pellets and heated at 923 K for 24 h. The samples obtained were again homogenized and pressed into pellets of 2.5 cm diam and 1–1.5 cm height, and heated at 1073 K for 12 h. All of the heating was carried out in air using a platinum crucible as a sample holder. The details of the sample characterization are given in the Supplemental Material.

A. Inelastic neutron scattering measurement

We used ~10 g of polycrystalline samples of Bi_2O_3, $(Bi_{0.8}Y_{0.2})_2O_3$, and $(Bi_{0.6}Y_{0.4})_2O_3$ to measure the phonon density of states (PDOS) at 323, 675, 900, and 1050 K. The measurements were carried out using the chopper spectrometer MARI, ISIS, UK, with continuous detector bank coverage ranging from 3 ° to 134 °. The measurements were conducted with 25 and 130 meV incident neutron energy to cover the Q range of 2–14 $Å^{-1}$ [50]. The measurements with $E_i = 130$ meV offer the complete spectrum, while those with $E_i = 25$ meV provide well-resolved low-energy (low-E) phonon modes. The neutron-weighted phonon density of states, $g^{(n)}(E)$, was obtained from the measured dynamic structure factor, $S(Q,E)$, as given by

$$g^{(n)}(E) = A\left\langle \frac{e^{2W(Q)}}{Q^2} \frac{E}{n(E,T) + \frac{1}{2} \pm \frac{1}{2}} S(Q,E) \right\rangle, \quad (1)$$

where A is a normalization constant, and Q, $2W$, and E are the momentum transfer, Debye-Waller factor, and phonon energy, respectively. $n(E,T)$ is the Bose-Einstein population factor for phonon energy E at temperature T. The +/– sign corresponds to the energy loss/gain of the neutron. The angular brackets in Eq. (1) represent the integration over Q. The measured $S(Q,E)$ depends on the temperature T. However, T does not occur on the left-hand side since the effect of T essentially cancels out when $S(Q,E)$ is divided by the phonon population $n(E,T)$.

The total neutron-weighted density of states, $g^{(n)}(E)$, is related to the atomic partial PDOS, $g_k(E)$, as follows:

$$g^{(n)}(E) = B \sum_k \left\{ \frac{4\pi b_k^2}{m_k} \right\} g_k(E). \quad (2)$$

Here B, b_k, and m_k are the normalization constant, the neutron scattering length, and the mass of the kth atom. Equation (2) gives the expression to obtain $g^{(n)}(E)$ from the calculated partial contribution of the constituent Bi and O atoms weighted by their scattering cross sections and their respective masses. The partial PDOS in Eq. (2) is obtained from the lattice dynamics calculations as well as from the AIMD simulations as described below.

B. Raman scattering measurement

The temperature-dependent Raman scattering measurements were carried out in the backscattering geometry using a Rieneshaw inVia^{TM} confocal Raman spectrometer equipped with a Peltier-cooled charge-coupled device detector. A diffraction grating of 2400 groves/mm provided a spectral resolution of <1 cm^{-1}. A 532 nm diode pumped solid state (DPSS) laser was used as an excitation source, and it was focused on the sample using a 10× objective with a laser power of <1 mW to avoid local heating. Initially, the spectrometer was calibrated with 521 cm^{-1} of Si thin film. A Linkam stage TS1500 with a temperature controller for the T-dependent measurements from 298 to 1033 K (± 0.1 K) was used. Using a low-wave-number filter that captures the signal close to the Rayleigh line, Raman spectra spanning a wide range from 23 to 1300 cm^{-1} were recorded. Finally, after applying the Bose-Einstein correction, we fit the obtained spectra using Lorentzian functions to calculate phonon energies (ω) and linewidths (Γ) at full width at half-maximum (FWHM).

C. *Ab initio* lattice dynamics and molecular dynamics simulation

We used density functional theory (DFT) for our lattice dynamics calculations and molecular dynamics simulations as implemented within the software package VASP (Vienna Ab-Initio Software Package) [52,53]. All the simulations were performed in the generalized gradient approximation (GGA) with the Perdew-Burke-Ernzerhof [54] (PBE) exchange-correlation functional and projected augmented wave (PAW)

pseudopotentials with a kinetic energy plane-wave cutoff of 900 eV. A single k-point sampling of the Brillouin zone at the zone center and an energy convergence of 10^{-6} eV were chosen.

The AIMD simulations were performed in the NVT ensemble using the Nose-Hoover thermostat [55]. A supercell [11] of $3 \times 2 \times 2$ dimensions with 240 atoms was used in the AIMD simulations of the monoclinic α-phase ($a = 5.934$ Å, $b = 8.29$ Å, and $c = 6.9377$ Å). The disordered δ-phases $(Bi_{1-x}Y_x)_2O_3$, $x = 0$, 0.2, 0.4, were modeled using a $3 \times 3 \times 3$ supercell ($a = 5.648$ Å) with 270 atoms in the supercell, and with requisite Bi replaced with Y using random numbers. The simulations were run for about 30–50 ps with 2 fs time steps. The initial 10 ps was used to attain the desired temperature and equilibration, and later trajectories were used for production.

The partial PDOS of the kth atom, $g_k(E)$, and the total PDOS, $g(E)$, were calculated from AIMD simulations by taking the Fourier transform of the velocity autocorrelation function [7],

$$g_k(E) = \frac{\int \boldsymbol{v}_k(0) \cdot \boldsymbol{v}_k(t) e^{iEt/\hbar} dt}{\langle \boldsymbol{v}_k(0) \cdot \boldsymbol{v}_k(0) \rangle}, \tag{3a}$$

$$g(E) = \sum_{k=1}^{N} g_k(E), \tag{3b}$$

where $v_k(t)$ is the kth atom velocity at time t, and N is the total number of atoms in the supercell. The partial PDOSs were also calculated from the lattice dynamics calculations using the atomic projections of the phonon eigenvectors [56]. The lattice dynamics calculations were performed for α-Bi_2O_3, δ-Bi_2O_3, and $(Bi_{0.75}Y_{0.25})_2O_3$. The calculations of the disordered cubic phase, as in the AIMD simulations, used a supercell.

The diffusion coefficient D can be estimated by different techniques, namely, using the mean-squared displacement (MSD), the velocity autocorrelation function (VACF), and the dynamical structure factor $S(Q,E)$. Here, we have calculated the time dependence of MSD using the following relationship:

$$\langle u^2(\tau) \rangle = \frac{1}{N_{\text{ion}}(N_{\text{step}} - N_\tau)} \sum_{i=1}^{N_{\text{ion}}} \sum_{j=1}^{N_{\text{step}}-N_\tau} |\boldsymbol{r}_i(t_j + \tau) - \boldsymbol{r}_i(t_j)|^2, \tag{4}$$

where $\boldsymbol{r}_i(t_j)$ is the ith atom position at the jth time step, $N_\tau = \tau/\delta$, δ being the time step in the simulation, N_{step} is the total number of simulation steps, and N_{ion} is the total number of a given element in a supercell. Using this time dependence, we estimated the T-dependent diffusivity D as given under the limit of large τ:

$$\langle D(T) \rangle = \langle u^2(\tau) \rangle / 6\tau. \tag{5}$$

The details of the calculation of the pair-distribution function, $g(r)$ [57,58], the van-Hove self-correlation function, $G_s(r,t)$ [59,60], and the O migration energy barrier, E_A [7], are explained in the Supplemental Material [35].

III. RESULTS AND DISCUSSIONS

A. Vibrational dynamics using inelastic neutron scattering and AIMD simulations

The low-energy dynamics in pure Bi_2O_3, $(Bi_{0.8}Y_{0.2})_2O_3$, and $(Bi_{0.6}Y_{0.4})_2O_3$ have been investigated to understand the onset of diffusion. Figure 1 gives the neutron spectrum, $S(E)$, integrated over the Q-range between 2 and 7 Å^{-1} using an incident neutron beam of $E_i = 25$ meV. It can be observed that in the case of Bi_2O_3, there is a well-defined inelastic peak structure above 2 meV with a clear separation from the elastic line at 323, 675, and 900 K. The first inelastic peak around 5 meV at 323 K gradually softens and broadens with an increase of the temperature. At 1050 K, the phonon peak structure significantly diminishes and a distinct broadening of the elastic line is evident, which implies an overdamped phonon structure. This change in the neutron spectrum from 900 to 1050 K coincides with the superionic phase transition from the monoclinic α-Bi_2O_3 to disordered cubic δ-Bi_2O_3 at 1003 K. A similar overdamped phonon structure is seen in the Y-doped compounds over 323–1050 K, which is consistent with the existence of the disordered cubic structure in these compounds over this temperature range.

The observed neutron spectrum is converted into the neutron-weighted PDOS using Eq. (1). Figures 2(a)–2(d) give the measured neutron-weighted PDOS with incident neutron energy of $E_i = 25$ meV. At 323 K, α-Bi_2O_3 shows a major low-E peak in PDOS at 7 meV. This feature is seen clearly in our simulations, as shown in Figs. 2(e)–2(h). As shown below from our simulations, the low-E peak involves the movement of both Bi and O atoms. Experimental spectra of $(Bi_{0.8}Y_{0.2})_2O_3$ and $(Bi_{0.6}Y_{0.4})_2O_3$ also show a significantly broad peaklike feature at 7 meV. The low-E peak around 7 meV broadens upon warming in all three compounds. The peak at 7 meV in α-Bi_2O_3 is seen clearly at 675 K, while it gets fairly broadened as the temperature rises to 900 K. Our simulations, too, show a clear peak around 7 meV in α-Bi_2O_3 up to 900 K as seen in Figs. 2(e)–2(h). However, the peak structure is lost in the disordered cubic δ-Bi_2O_3 at 1050 K, as well as in the Y-stabilized disordered cubic $(Bi_{0.8}Y_{0.2})_2O_3$ and $(Bi_{0.6}Y_{0.4})_2O_3$ at all temperatures. At 1050 K, δ-Bi_2O_3 shows increased densities at the low-E region followed by $(Bi_{0.8}Y_{0.2})_2O_3$, and then the least density is seen in $(Bi_{0.6}Y_{0.4})_2O_3$. These features are brought out well in our simulations, as shown in Figs. 2(e)–2(h).

The phonon spectrum measured using $E_i = 130$ meV shows a significant broadening in the entire spectral range upon warming, and it infers an overall anharmonic behavior of phonons (Fig. S3 [34]). Our temperature-dependent calculated PDOSs using AIMD trajectories are in tandem with the experimental observations (Fig. S4 [34]). From the above discussions, we can surmise that in the δ-phase, the distinct phonon signatures of the α-phase are lost with considerable phonon broadening. This broadening increases with increased Y fraction from 20% to 40%, and we can see that there are broad phonon peaks seen in $(Bi_{0.8}Y_{0.2})_2O_3$, which are further broadened and appear indiscernible in the case of $(Bi_{0.6}Y_{0.4})_2O_3$. This increased broadening is due to oxygen positional disorder and anharmonicity.

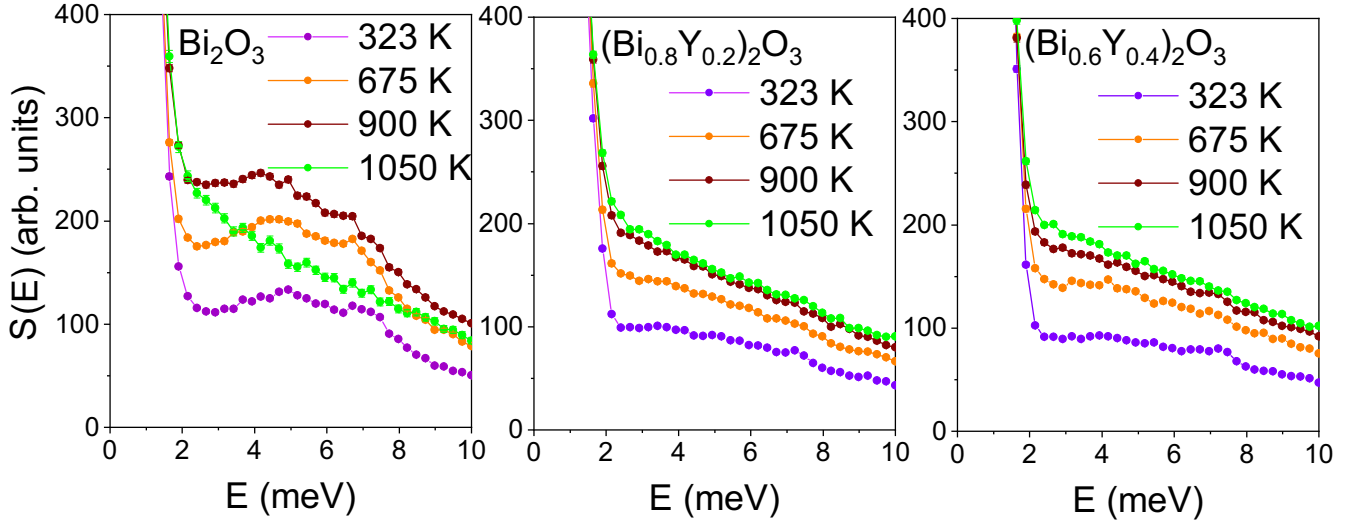

FIG. 1. Measured $S(E)$ integrated over $Q(2–7\ \text{Å}^{-1})$ for incident $E_i = 25$ meV in undoped Bi_2O_3, $(Bi_{0.8}Y_{0.2})_2O_3$, and $(Bi_{0.6}Y_{0.4})_2O_3$ with increasing temperature.

Further, to obtain a clear understanding of the changes occurring in the superionic regime, we have plotted the partial PDOS of Bi and O (computed from AIMD simulations) in Fig. 3 at 1000 K between 0 and 10 meV. We see that the low-E spectra of both Bi and O in δ-Bi_2O_3 at 1000 K are shifted to lower energies compared to that in the α-Bi_2O_3 at 900 K. This indicates that the Bi and O dynamics are coupled, and Bi dynamics strongly influence oxygen diffusion in δ-Bi_2O_3 (explicitly shown later). We note that, in the low-E regime, the partial PDOS of Bi in the Y-doped Bi_2O_3 is quite similar to that in δ-Bi_2O_3 and is larger compared to that in α-Bi_2O_3. Interestingly, the oxygen PDOS in the low-E regime shows the largest density in δ-Bi_2O_3, followed by $(Bi_{0.8}Y_{0.2})_2O_3$, $(Bi_{0.6}Y_{0.4})_2O_3$, and α-Bi_2O_3.

The calculated partial PDOSs in the energy range of 0–130 meV are shown in Fig. S5. In all the compounds, oxygen contributes throughout the entire energy spectrum, with its peaks moving to lower energies upon heating. Bi primarily

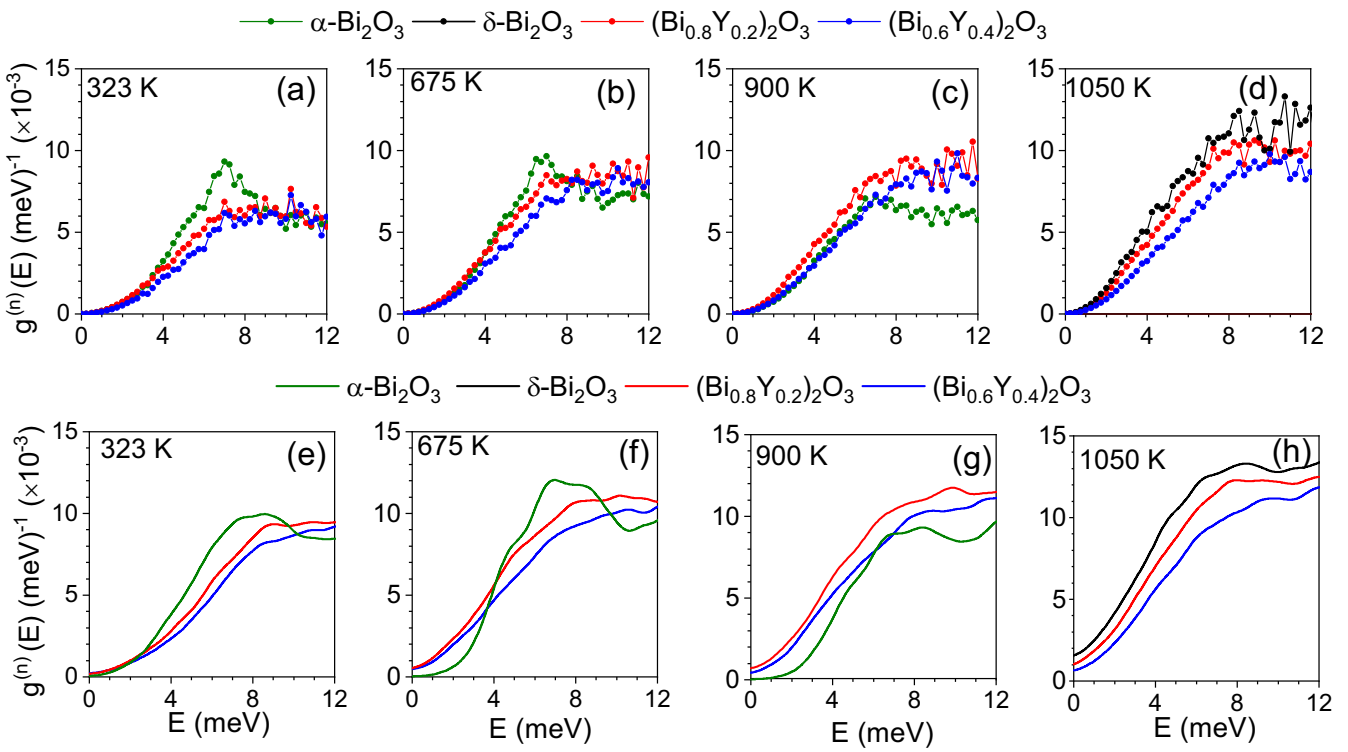

FIG. 2. (a)–(d) The experimental data of the neutron-weighted phonon density of states, $g^{(n)}(E)$, of undoped and doped Bi_2O_3 with increasing temperature. (e)–(h) AIMD simulated PDOS for the different oxides with increasing temperature. The experimental PDOSs at each temperature were normalized with respect to the respective calculated PDOS.

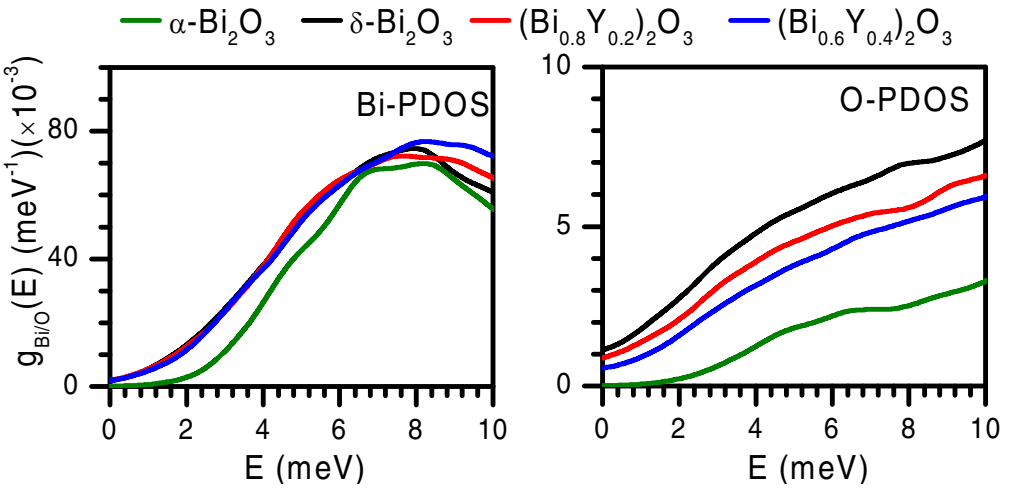

FIG. 3. AIMD simulated partial PDOS of Bi and O in δ-Bi_2O_3 and Y-doped $(Bi_{0.8}Y_{0.2})_2O_3$ and $(Bi_{0.6}Y_{0.4})_2O_3$ oxides at 1000 K, and in α-Bi_2O_3 at 900 K.

contributes below 20 meV, and Y contributes below 40 meV in doped oxides. Further, the calculated oxygen PDOS shows a finite density at 0 meV at high temperatures, implying the presence of diffusion [50,61–63].

The INS studies on polycrystalline samples are very useful to obtain an overall picture of the phonon energy distribution over the entire Brillouin zone. The temperature effect on specific phonon modes at the Brillouin zone center across the superionic transition has been investigated by Raman spectroscopy as discussed below.

B. Raman scattering measurements

Using Raman scattering, our interest is to investigate individual phonon behavior and its possible role in O diffusion. We also wished to study the changes occurring in the Raman scattering due to variable Y-doping; hence we performed temperature-dependent Raman measurements in Bi_2O_3, and Y-doped Bi_2O_3 from room temperature to 1003 K. The room-temperature Raman spectrum of Bi_2O_3 (α-Bi_2O_3) shows sharp peaks below 200 cm^{-1} and broad features above 200 cm^{-1}, as shown in Fig. 4(a). The peak around 525 cm^{-1} is barely discernible. Our measurements are consistent with that reported by Yaffe *et al.* [28]. A number of Raman peaks were observed between 40 and 230 cm^{-1} (region 1, R1), between 275 and 325 cm^{-1} (region 2, R2), and between 400 and 460 cm^{-1} (region 3, R3). As the temperature increases to 373 K, the peaks broaden; upon further heating, the low-E peaks gradually broaden. The broadening of the peaks in the R1 region is much smaller, in excellent agreement with the spectra reported by Betsch *et al.* [31], and individual peaks are distinguishable up to temperatures of 953 K. The low-E phonons in the R1 region have a nearly equal contribution of Bi and O atoms [see Fig. 4(b)]. Despite increased O diffusion at high-T, the Bi host sublattice remains intact. Consequently, peaks are relatively well-defined even at high-T. Between 523 and 893 K, all the peaks beyond 200 cm^{-1} are significantly broadened. Beyond 150 cm^{-1}, some of the frequencies have coalesced with each other. The peak around 445 cm^{-1}, seen clearly at room temperature, shifts slowly to the lower side and disappears beyond 973 K, where only a few peaks below 150 cm^{-1} were observable.

In Y-doped Bi_2O_3, broad peaklike structures are observed below 200 cm^{-1} and around 620 cm^{-1} [Fig. 4(a)]. Many closely spaced Raman active modes give rise to these broad features in the doped oxides. This is due to the formation of different local structures around the Bi/Y atoms due to random substitution at some of the Bi sites by Y atoms in the Y-doped systems. These peaks get progressively broadened but remain persistent up to 1013 K, beyond which data could not be measured as the sample melted. The persistence of peaks is again due to the stability of the host Bi/Y sublattice. The temperature evolution of the Raman peaks around 106 and 620 cm^{-1} in the two doped samples has been plotted and compared in Fig. S6 [34]. Modes beyond 550 cm^{-1} seen in the Raman data of the Y-doped samples are not seen in δ-Bi_2O_3 [Fig. 4(a)]. With the introduction of Y, there may be changes in the microscopic local structure. Hence, we surmise that it is plausible that changes brought about by Y-doping might have made these higher energy modes Raman active, which were Raman inactive in the undoped Bi_2O_3.

Further, in the undoped δ-Bi_2O_3 (Fig. S1 [34]) and the Y-substituted system, all oxygen sites are equivalent. However, in the Y-doped structure, there are a few oxygens closer to a Bi/Y atom as compared to other oxygen atoms. Figure S7 [34] gives the eigenvectors of a few selected modes in the different Bi_2O_3 and doped Bi_2O_3 oxides in the simulated cell. From these displacement patterns, we can see that certain oxygen atoms closer to Bi/Y display higher amplitudes compared to the other oxygen atoms, implying a much shallower potential in their vicinity, leading to the onset of O hopping at a lower temperature. This observation appears in conjunction with the lattice dynamics calculated contribution of phonon energy E to the mean-squared displacements of various atoms at 300 K, averaged over the entire Brillouin zone in α-Bi_2O_3, δ-Bi_2O_3, and $(Bi_{0.75}Y_{0.25})_2O_3$ [Fig. 4(b)].

To get a cumulative picture of the role of phonons in the thermal amplitude of various atoms in the pure α- and δ-phases of Bi_2O_3 and in 25% Y-doped Bi_2O_3, we have plotted the variation of $\langle u^2 \rangle$ with phonon energies averaged over the

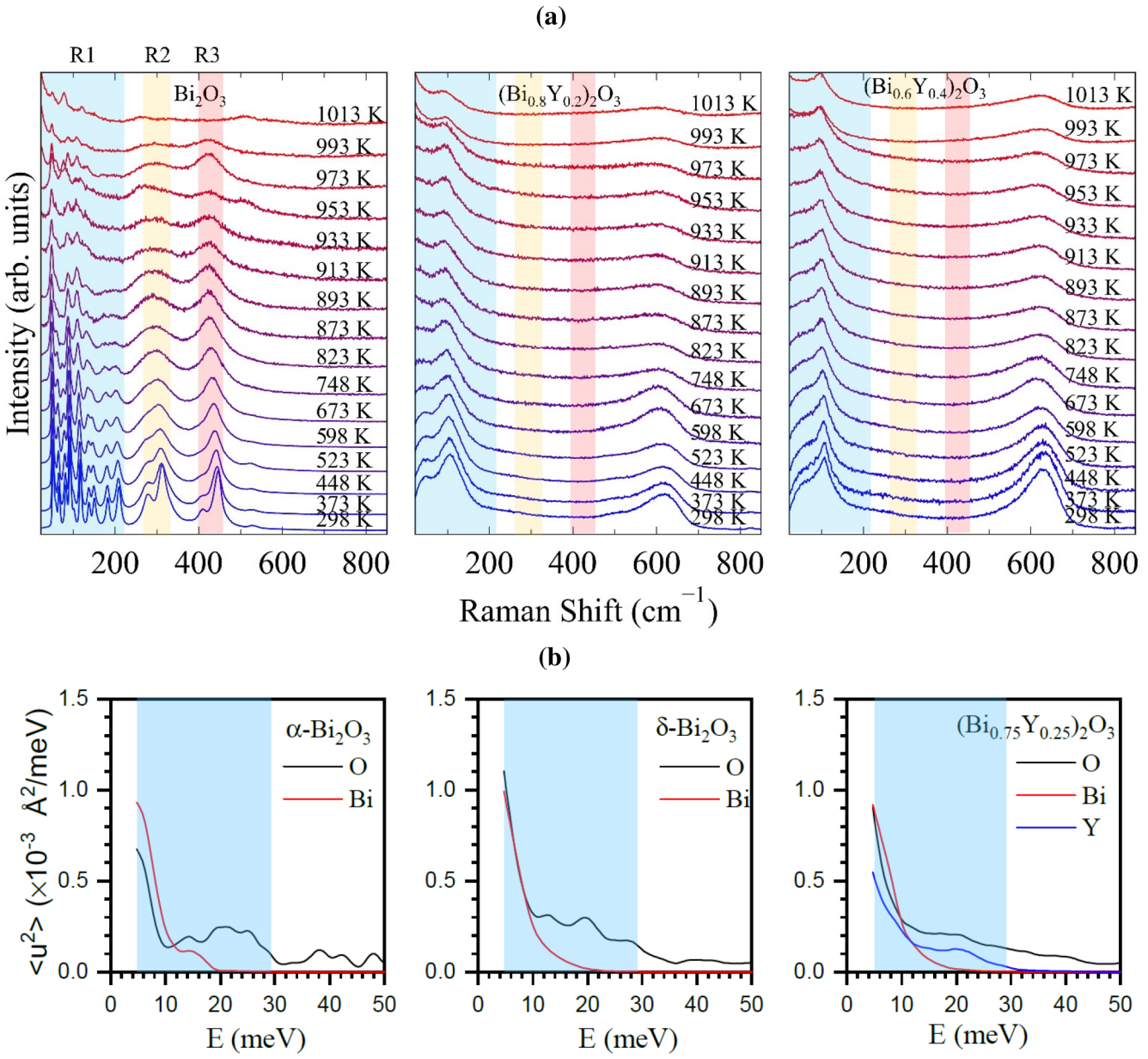

FIG. 4. (a) Raman spectra measured in α and δ phases of undoped Bi_2O_3 at different temperatures and in the 20% and 40% Y-doped $(Bi_{0.8}Y_{0.2})_2O_3$ and $(Bi_{0.6}Y_{0.4})_2O_3$ oxides at different temperatures. The regions R1, R2, and R3 discussed in the text have been marked in different colors. (b) The lattice dynamics calculated contribution of phonon energy E to the mean-squared displacements of various atoms at 300 K, averaged over the entire Brillouin zone in α-Bi_2O_3, δ-Bi_2O_3, and $(Bi_{0.75}Y_{0.25})_2O_3$. 1 meV = 8.06 cm^{-1}. Region R1 is marked in blue.

entire Brillouin zone at 300 K [see Fig. 4(b)]. We find that the amplitude of Bi is higher for low-energy phonons below 10 meV in α-Bi_2O_3, while in the high-energy range, oxygen atoms show higher amplitudes. Clearly, the Bi dynamics plays an important role in low-E phonons in the monoclinic phase. In the case of δ-Bi_2O_3 and $(Bi_{0.75}Y_{0.25})_2O_3$, the amplitudes of O and Bi are comparable in the low-E phonons below 10 meV, beyond which oxygen amplitudes are higher than Bi and Y. In the Y-doped compound, $\langle u^2 \rangle$ of Y is higher than Bi between 15 and 25 meV. The vibration of Y could be facilitating local distortions in the lattice at the microscopic level such that the barrier for oxygen diffusion might be lowered. This appearance of shallower potential might help in oxygen hopping. Hence, it is possible that this extra $\langle u^2 \rangle$ of Y is one of the factors leading to the exhibition of increased oxygen diffusion in these Y-doped compounds (shallower potential to hop) at temperatures (~700 K) well below the fast ion transition temperature (1003 K) of the pure δ-phase. We expand on this point later in the text.

Having carried out studies on the behavior of phonons in the entire Brillouin zone as well as on individual phonons at the zone center with increasing temperature, we found overall anharmonicity at elevated temperatures and identified the disappearance of a few phonon modes upon the onset of oxygen diffusion. Now to microscopically understand the role of structure and host-dynamics in the diffusion of oxide ions, we have carried out detailed AIMD simulation studies as discussed below.

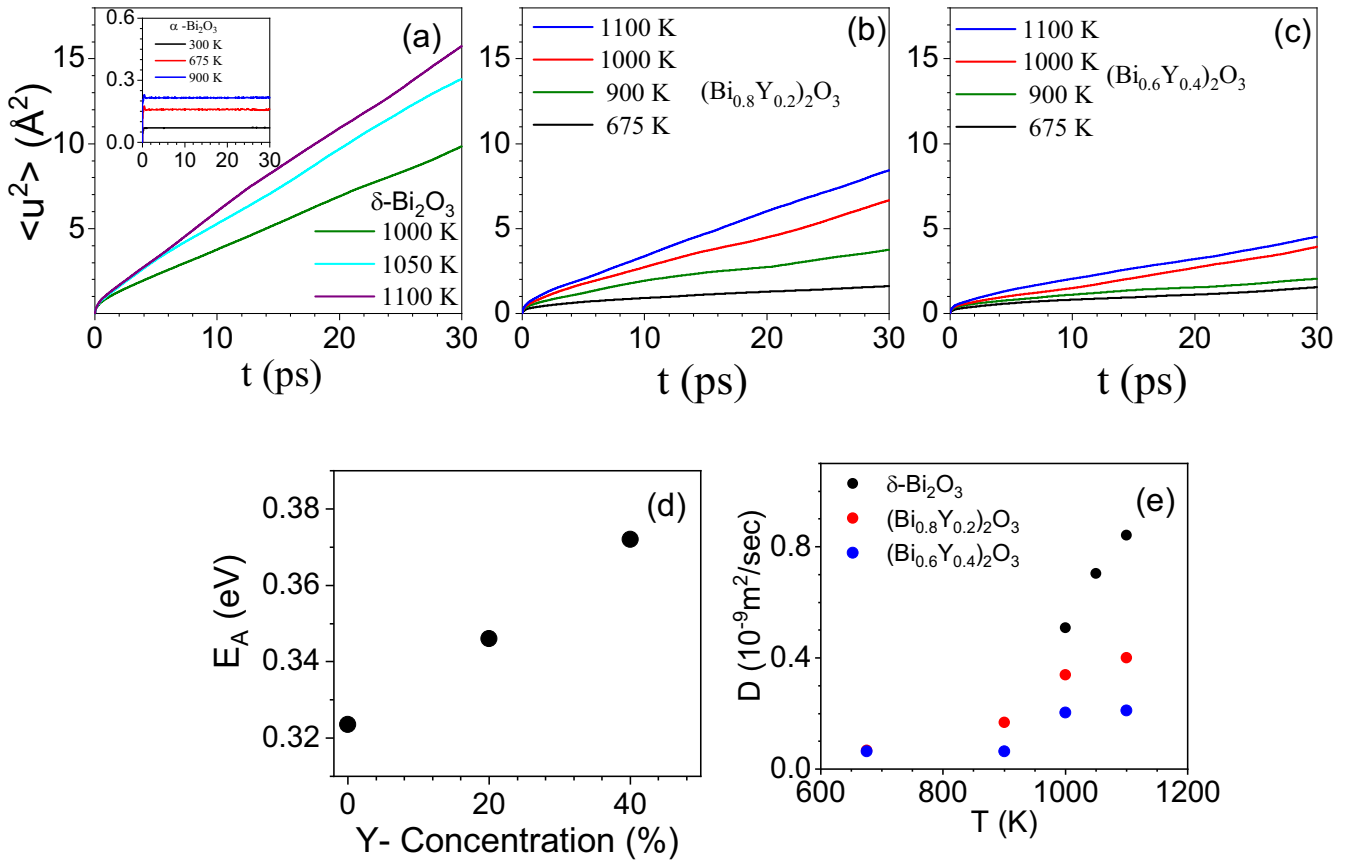

FIG. 5. (a)–(c) AIMD simulated mean-square displacement of oxygen in undoped and doped Bi_2O_3. (d) Variation of activation energy (E_A) for oxygen diffusion with increasing concentration of Y. Activation energies have been obtained from the free-energy landscape of oxygen ions, as calculated from the probability of occupancy of the oxygen atom. (e) Diffusion coefficient in disordered δ-Bi_2O_3, $(Bi_{0.8}Y_{0.2})_2O_3$, and $(Bi_{0.6}Y_{0.4})_2O_3$ with increasing temperature.

C. Role of structure and dynamics in oxygen diffusion

1. Oxygen diffusion

To investigate the characteristics of diffusion processes, we analyze the AIMD trajectories. We compute the mean-squared displacement (MSD) at temperatures from 300 to 1100 K in the undoped and the Y-doped structures [Figs. 5(a)–5(c)]. The host elements (Bi,Y) in all the structures show nearly time-independent MSD, which infers a stable host lattice formed by (Bi,Y). In the α-Bi_2O_3, the MSD of O also remains time-independent and does not exhibit any diffusion even up to 900 K. However, the MSD of O atoms in the δ-Bi_2O_3 structure shows significant oxygen diffusion at 1000 K and above [Figs. 5(a)–5(c)]. There is about a 5% increase in volume from α-Bi_2O_3 to δ-Bi_2O_3 at the phase transition. To see the explicit effect of volume on oxygen diffusion, we performed the AIMD simulation in α-Bi_2O_3 with expanded volume (∼5%) at 1000 K, but we did not observe the oxygen diffusion [Fig. S8(a) [34]]. This clearly shows that the host structure of δ-Bi_2O_3 is critical for O diffusion.

Interestingly, in Y-doped Bi_2O_3, i.e., $(Bi_{0.8}Y_{0.2})_2O_3$ and $(Bi_{0.6}Y_{0.4})_2O_3$, we observe significant O diffusion below 1000 K, which is absent in α-Bi_2O_3. Earlier AIMD simulation on $(Bi_{0.7}Y_{0.3})_2O_3$ also indicated the onset of oxygen diffusion at lower temperatures [50]. The onset of O diffusion at lower temperatures could be caused by the cubic-framework structure and the presence of anharmonic low-E host-lattice vibrations (below 4 meV) in Y-doped Bi_2O_3, which is strongly suppressed in α-Bi_2O_3. The diffusion coefficient of oxygen has been estimated from MSD using the Einstein relation [see Fig. 5(e)]. The diffusion of O in $(Bi_{0.8}Y_{0.2})_2O_3$ and $(Bi_{0.6}Y_{0.4})_2O_3$ begins in AIMD at around 675 K, which is significantly lower than ∼1000 K in the stability regime of undoped δ-Bi_2O_3 as seen from Fig. 5(e).

Further, we have estimated the barrier energy for oxygen diffusion in δ-Bi_2O_3 and Y-doped Bi_2O_3 at 1000 K using O probability density [7] as shown in [Fig. 5(d)]. Interestingly, the barrier energy increases with Y concentration. As noted above, Y doping stabilizes the cubic phase at lower temperatures, which provides many vacant sites and facilitates oxygen migration. Hence, there is a tradeoff between superionic cubic structure stability vs barrier energy, and it is apparent that ∼20% Y doping is well suited for the O diffusion, and larger Y doping leads to reduced O diffusion. At a 20% substitution level, Y stabilizes the cubic phase and allows easy migration for O through channels formed by the Bi-Y network. In comparison, at a higher concentration of 40%, the channels formed are narrower, which hinders the O diffusion. To get an overview of the diffusing oxygen atoms, we show the calculated oxygen probability isosurface plots at 1000 K in Fig. 6. It is clearly seen from the extensive connections in the isosurface plot (yellow dots) that oxygen diffuses copiously in δ-Bi_2O_3

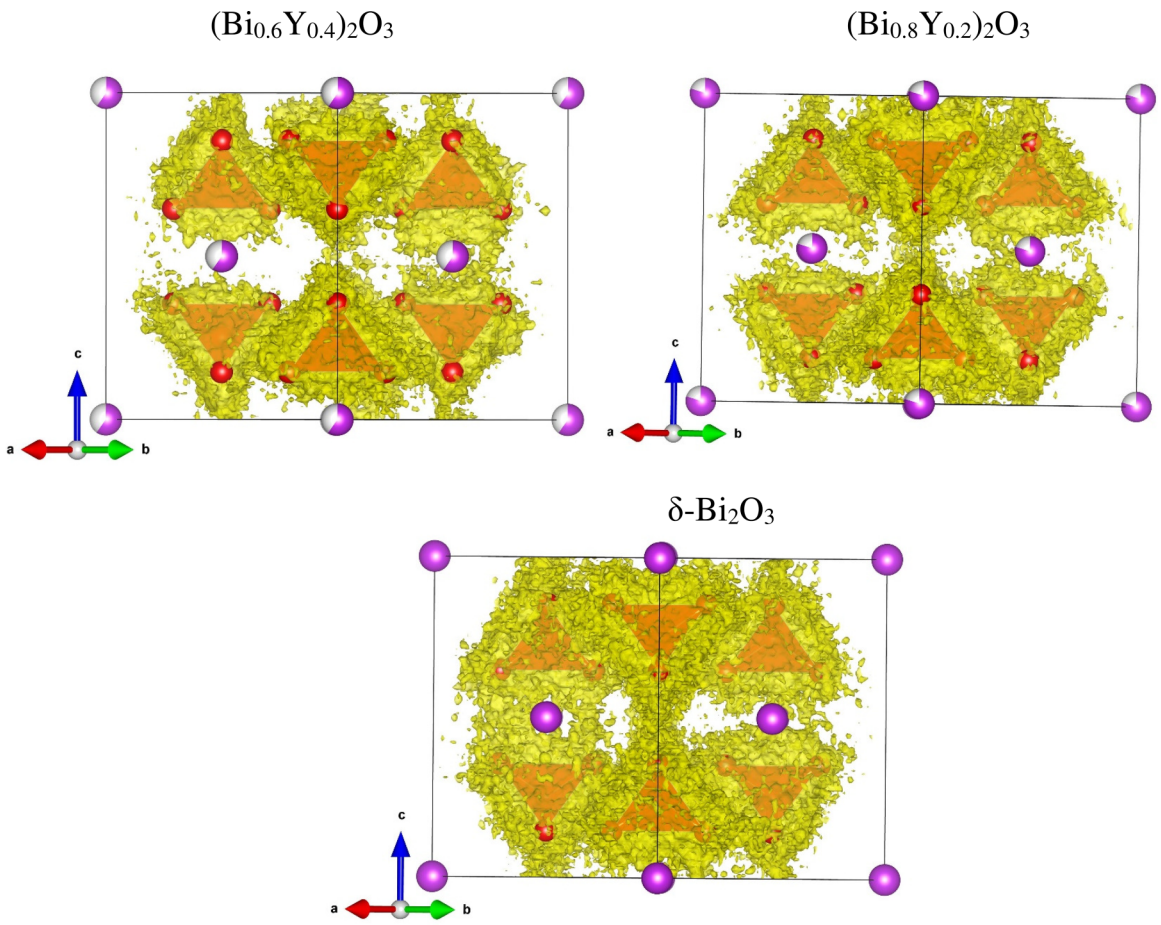

FIG. 6. Oxygen probability isosurface plot (isosurface value = 0.005 $Å^{-3}$) (in yellow dots) at 1000 K corresponding to $(Bi_{0.6}Y_{0.4})_2O_3$, $(Bi_{0.8}Y_{0.2})_2O_3$, and δ-Bi_2O_3, respectively. The oxygen sites forming tetrahedral clusters are shown in red; purple-white spheres correspond to the Bi/Y atom's partial occupancies.

followed by $(Bi_{0.8}Y_{0.2})_2O_3$ and least in $(Bi_{0.6}Y_{0.4})_2O_3$, which is in concurrence with their respective diffusion coefficients.

To explicitly investigate the role of host dynamics on the diffusion of oxygen, we performed the AIMD simulation in δ-Bi_2O_3 with the frozen host (i.e., fixed Bi positions) at 1000 K. We find that upon freezing of Bi, O diffusion reduces by nearly an order of magnitude [see Fig. S8(b) [34]]. These simulations reiterate that the cubic structure of δ-Bi_2O_3 is critical for O diffusion in Bi_2O_3, and host vibrations accelerate oxygen diffusion.

2. Pair distribution function and the van Hove correlations

We have calculated the pair distribution function, $g(r)$ (Figs. 7 and S9 [34]), of different O-O, Bi-O, and Bi-Bi pairs in α-Bi_2O_3 at 900 K and δ-Bi_2O_3 at 1100 K. We can see a significant change in the first-neighbor peak in the Bi-Bi PDF in δ-Bi_2O_3 compared to α-Bi_2O_3, inferring that the average structure of δ-Bi_2O_3 is quite different. The average Bi-Bi peak position in α-Bi_2O_3 occurs at a lower distance (3.7 Å) than the Bi-Bi site distance (3.9 Å) in δ-Bi_2O_3, indicating that Bi forms a more open-structure framework in δ-Bi_2O_3, thus assisting in fast oxygen diffusion. It may be noted that we do not see a significant change in Bi-Bi PDF between the cubic and Y-doped Bi_2O_3 oxides. In the case of O-O PDF, α-Bi_2O_3 shows a broad peak, while in the other three oxides, it is broader and has an asymmetric distribution. The first-neighbor O-O distance in δ-Bi_2O_3 and Y-doped oxides is around 3 Å, while in the case of α-Bi_2O_3 it is at 3.2 Å. The first-neighbor Bi-O distance is almost the same for all the oxides, i.e., ∼2.25 Å.

To investigate the jump-length distributions and time evolution of oxygen hops, we have computed the van Hove self-correlation function $g_s(r,t)[= G_s(r,t) * 4\pi r^2]$ for O in the δ-Bi_2O_3 and the Y-doped structures at 1000 K and α-Bi_2O_3 at 900 K (Fig. 8). In diffusing systems, the peaks in the van Hove self-correlation strongly decay with time. However, in the present case of α-Bi_2O_3 at 900 K, we do not see any visible change in the peak intensity (at ∼0.5 Å) with time, which confirms the absence of O diffusion as corroborated by the MSD behavior. In the case of δ-Bi_2O_3, the first peak is around 0.9 Å and the second peak is around 2.2 Å at 4 ps. In δ-Bi_2O, O-O intersite distances lie from 1.64 to 4.33 Å; this results in multiple possibilities of jump length. We observed that the $g_s(r,t)$ second peak gradually broadens as time increases; O atoms may jump from one site to another due to covering all possible intersite jump-distances and resembling a liquidlike diffusion (Fig. S10 [34]). We find that there are two distinct peaks in the case of the three oxides: (i) for δ-Bi_2O_3, the first peak is at around 0.88 Å,

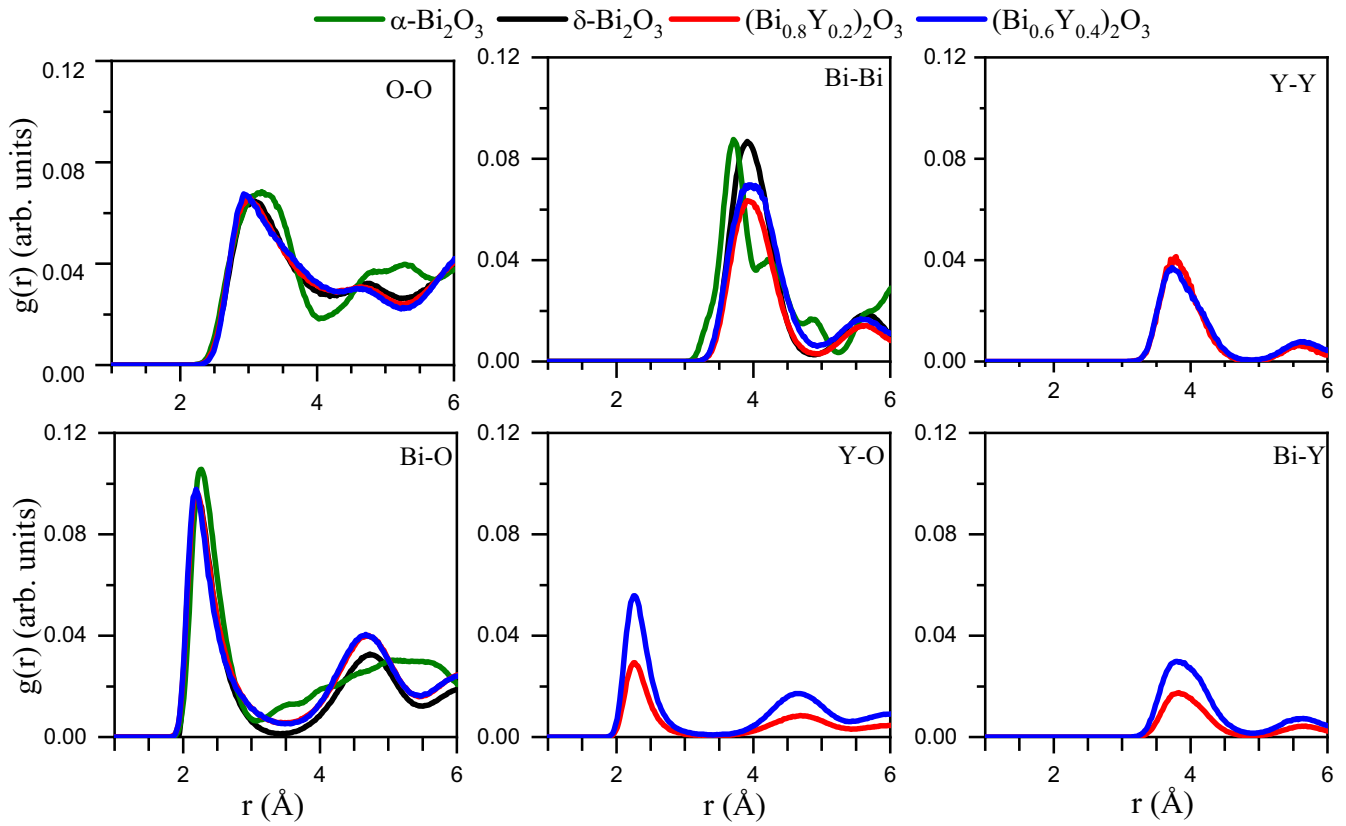

FIG. 7. Pair distribution function $g(r)$ at 1100 K for δ-Bi_2O_3, $(Bi_{0.8}Y_{0.2})_2O_3$, and $(Bi_{0.6}Y_{0.4})_2O_3$, and at 900 K for α-Bi_2O_3.

while the second peak is at around 3.1 Å; (ii) in the case of $(Bi_{0.8}Y_{0.2})_2O_3$, the first peak is around 0.73 Å, while the second is around 2.9 Å; and (iii) in the case of $(Bi_{0.6}Y_{0.4})_2O_3$, the first peak is around 0.62 Å and the second is around 2.5 Å. Clearly, as the Y substitution is increased, the jump distances are reduced.

3. *Probability distribution of* $(Bi/Y)_4O$ *tetrahedra*

It is still unclear which feature of the structure prevents oxygen in the α-Bi_2O_3 phase from diffusing even at 1000 K. We explore this question below. As the diffusion naturally depends on the empty volume available around the O atom, we focus on the volume of the $(Bi/Y)_4O$ tetrahedral units. In α-Bi_2O_3, there are two symmetrically distinct Bi-sites, which lead to three different kinds of Bi_4O tetrahedral units with peak volumes centered at ~6.4, 6.8, and 7.5 $Å^3$, respectively. In contrast, in the disordered structures of δ-Bi_2O_3, $(Bi_{0.8}Y_{0.2})_2O_3$, and $(Bi_{0.6}Y_{0.4})_2O_3$, Bi and Y form an edge-sharing tetrahedral framework of $(Bi/Y)_4O$. In Figs. 9 and S11 [34], we have shown the time-averaged tetrahedral volume distribution at 1000 K in the various phases and with different degrees of Y-doping from AIMD simulations. The peak values of distribution corresponding to the Bi_4O tetrahedral volume in δ-Bi_2O_3, $(Bi_{0.8}Y_{0.2})_2O_3$, and $(Bi_{0.6}Y_{0.4})_2O_3$ are around 7.2, 7.1, and 6.9 $Å^3$, respectively. It can be seen that these values are larger than the peak value of ~6.9 $Å^3$ seen in α-Bi_2O_3. Hence, we infer that the average-tetrahedral volume

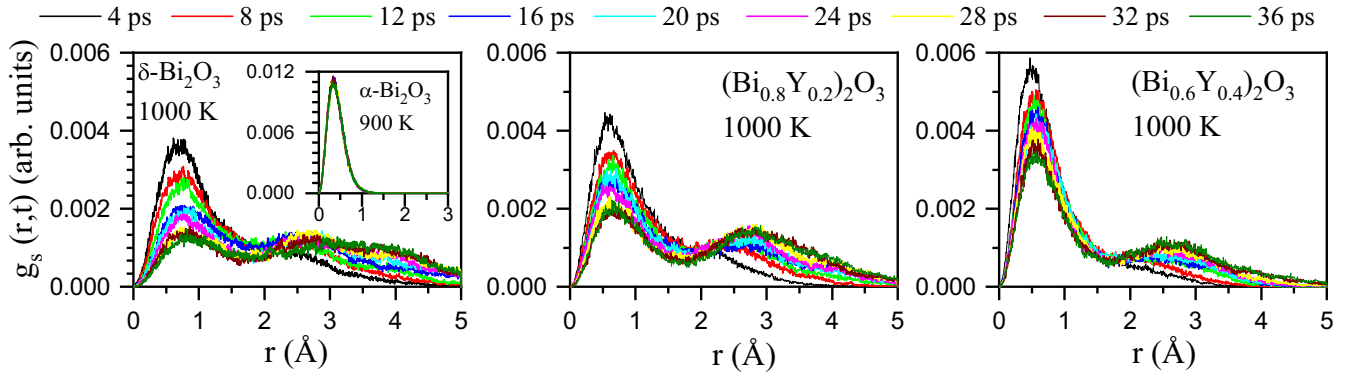

FIG. 8. The AIMD calculated O-atom van Hove self-correlation function $g_s(r,t)[= G_s(r,t)^*4\pi r^2]$ of δ-Bi_2O_3, $(Bi_{0.8}Y_{0.2})_2O_3$, and $(Bi_{0.6}Y_{0.4})_2O_3$ at 1000 K. The inset shows the function for α-Bi_2O_3 at 900 K.

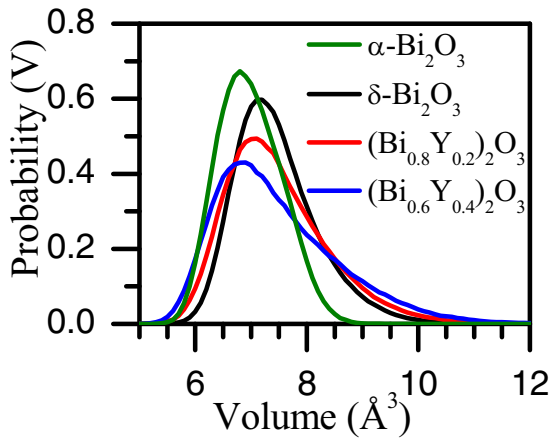

FIG. 9. Distribution of Bi_4O tetrahedral volume in δ-Bi_2O_3, $(Bi_{0.8}Y_{0.2})_2O_3$, $(Bi_{0.6}Y_{0.4})_2O_3$, and α-Bi_2O_3.

is correlated with the O diffusion coefficients. In α-Bi_2O_3, a smaller tetrahedral Bi_4O unit leads to a large barrier energy for O hops. It closes the tetrahedral percolating pathways, leading to the hindrance of O diffusion. The above results indicate that the size and distribution of Bi_4O tetrahedra have an interesting impact on O diffusion. Our observations agree with the results of Battle *et al.* [49] that doping increases the resistance to the free O diffusion. The larger the volume of the tetrahedra, the better is the diffusion. The microscopic changes occurring in the Bi and O sublattice profoundly affect the possibility of O diffusion as we go from fully ordered monoclinic α-phase to Y-doped δ-Bi_2O_3 with varying concentrations and then finally to the disordered undoped δ-phase.

IV. CONCLUSIONS

We have carried out detailed inelastic neutron scattering and Raman scattering studies on the effect of doping and temperature on the vibrational response of Bi_2O_3 and $(Bi_{1-x}Y_x)_2O_3$ ($x = 0.2, 0.4$). We find a pronounced change in the PDOS across the transition from the monoclinic α-phase to the disordered cubic δ-phase at ~1003 K. The PDOS and Raman spectra reveal the overall phonons in the δ-phase to be highly anharmonic. Our calculations and experiments show that the phonon spectra in the doped systems at 675 K follow the anharmonic characteristics of the disordered cubic δ-phase of the undoped system above 1003 K.

We have studied the undoped and two Y-doped Bi_2O_3 with 20% and 40% doping levels. From our studies, we find that the 20% Y-doping is the best among the three samples for oxygen ionic conduction at low temperatures. Our simulations also reveal that a larger volume of average Bi_4O tetrahedra favors faster oxygen diffusion. The largest volume of average Bi_4O tetrahedra is found for the 20% Y-doping among the three samples studied.

We have also performed simulations on the frozen Bi host-lattice of a cubic disordered δ-phase that show suppressed oxygen diffusion, revealing the host dynamics' importance in diffusion. Hence, an interplay among phonon anharmonicity, flexible host-dynamics, and vacant sites dictates the oxygen diffusion in Bi_2O_3 and Y-doped oxides.

ACKNOWLEDGMENTS

The use of ANUPAM supercomputing facility at BARC is acknowledged. S.L.C. acknowledges the financial support of the Indian National Science Academy for the INSA Senior Scientist position. R.M. and P.G. thank the Department of Science and Technology, India (SR/NM/Z-07/2015) for the financial support and Jawaharlal Nehru Centre for Advanced Scientific Research (JNCASR) for managing the project. Experiments at the ISIS Neutron and Muon Source were supported by beam time allocations RB 1920321 from the Science and Technology Facilities Council. The authors acknowledge the use of the Raman scattering facility at IITB, and A.P.R. and D.B. gratefully acknowledge the financial support from Science & Engineering Research Board (SERB) under Project No. CRG/ 2022/ 001317 and MoE/ STARS under Project No. MoE/ STARS- 1/ 345.

[1] F. Schröder, N. Bagdassarov, F. Ritter, and L. Bayarjargal, Phase Trans. **83**, 311 (2010).
[2] E. Mamontov, Solid State Ion. **296**, 158 (2016).
[3] M. Coduri, M. Karlsson, and L. Malavasi, J. Mater. Chem. A **10**, 5082 (2022).
[4] G. Paściak, J. Chmielowiec, and P. Bujło, Mater. Sci.–Poland **23**, 209 (2005).
[5] M. K. Gupta, J. Ding, N. C. Osti, D. L. Abernathy, W. Arnold, H. Wang, Z. Hood, and O. Delaire, Energy Environ. Sci. **14**, 6554 (2021).
[6] S. Kumar, M. K. Gupta, P. Goel, R. Mittal, S. Mukhopadhyay, M. D. Le, R. Shukla, S. N. Achary, A. K. Tyagi, and S. L. Chaplot, J. Mater. Chem. A **11**, 1712 (2023).
[7] M. K. Gupta, S. Kumar, R. Mittal, and S. L. Chaplot, Phys. Rev. B **106**, 014311 (2022).
[8] M. K. Gupta, J. Ding, D. Bansal, D. L. Abernathy, G. Ehlers, N. C. Osti, W. G. Zeier, and O. Delaire, Adv. Energy Mater. **12**, 2200596 (2022).
[9] S. Hull, S. T. Norberg, M. G. Tucker, S. G. Eriksson, C. E. Mohn, and S. Stølen, Dalton Trans. 8737 (2009).
[10] K. Rawat, D. D. Fong, and D. S. Aidhy, J. Appl. Phys. **129**, 095301 (2021).
[11] A. Togo and I. Tanaka, Scr. Mater. **108**, 1 (2015).
[12] C. E. Mohn, S. Stølen, S. T. Norberg, and S. Hull, Phys. Rev. B **80**, 024205 (2009).
[13] C. E. Mohn and M. Krynski, Phys. Rev. B **101**, 104309 (2020).
[14] A. Toda and S. Kishimoto, IEEE Trans. Nucl. Sci. **70**, 164 (2023).
[15] Q. Xiao, J. Zhu, C. Cheng, J. Liu, X. Zhang, Z. Li, and J. Zhu, Nanoscale **15**, 3884 (2023).

[16] A. V. Chadwick, in *Diffusion in Materials*, edited by A. L. Laskar, J. L. Bocquet, G. Brebec, and C. Monty (Springer Netherlands, Dordrecht, 1990), pp. 489–518.
[17] W. Zhang and M. Yashima, Chem. Commun. **59**, 134 (2023).
[18] J. Janek and W. G. Zeier, Nat. Energy **8**, 230 (2023).
[19] R. Punn, A. M. Feteira, D. C. Sinclair, and C. Greaves, J. Am. Chem. Soc. **128**, 15386 (2006).
[20] P. Battle, G. Hu, L. Moroney, and D. Munro, J. Solid State Chem. **69**, 30 (1987).
[21] H. Kruidhof, K. De Vries, and A. Burggraaf, Solid State Ion. **37**, 213 (1990).
[22] A. Dapčević, A. Radojković, M. Žunić, M. Počuča-Nešić, O. Milošević, and G. Branković, Sci. Sintering **53**, 55 (2021).
[23] I. Jeong, S. J. Jeong, B.-H. Yun, J.-W. Lee, C.-W. Lee, W. Jung, and K. T. Lee, NPG Asia Mater. **14**, 53 (2022).
[24] A. Borowska-Centkowska, X. Liu, M. Krynski, M. Leszczynska, W. Wrobel, M. Malys, S. Hull, S. T. Norberg, F. Krok, and I. Abrahams, RSC Adv. **9**, 9640 (2019).
[25] P. S. Cardenas-Terrazas, M. T. Ayala-Ayala, J. Muñoz-Saldaña, A. F. Fuentes, D. A. Leal-Chavez, J. E. Ledezma-Sillas, C. Carreño-Gallardo, and J. M. Herrera-Ramirez, Ionics **26**, 4579 (2020).
[26] M. Balci and M. Ari, J. Mater. Sci. Mater. Electron. **34**, 534 (2023).
[27] A. Alshoaibi, F. Hussain, F. Mohsin, N. Alnaim, and N. Almulhem, Front. Mater. **10**, 1004889 (2023).
[28] R. Sharma, N. Benshalom, M. Asher, T. M. Brenner, A. Kossi, O. Yaffe, and R. Korobko, arXiv:2205.13289.
[29] S. Narang, N. Patel, and V. Kartha, J. Mol. Struct. **327**, 221 (1994).
[30] A. Pereira, O. Gomis, J. Sans, J. Pellicer-Porres, F. Manjón, A. Beltran, P. Rodríguez-Hernández, and A. Muñoz, J. Phys.: Condens. Matter **26**, 225401 (2014).
[31] R. J. Betsch and W. B. White, Spectrochim. Acta Part A: Mol. Spectrosc. **34**, 505 (1978).
[32] L. Loubbidi, M. Naji, B. Orayech, A. Chagraoui, J. Igartua, A. Moussaoui, and A. Tairi, Orient. J. Chem. **32**, 47 (2016).
[33] H. Cahen, T. Van Den Belt, J. De Wit, and G. Broers, Solid State Ion. **1**, 411 (1980).
[34] D. S. Aidhy, S. B. Sinnott, E. D. Wachsman, and S. R. Phillpot, Ionics **16**, 297 (2010).
[35] See Supplemental Material at http://link.aps.org/supplemental/10.1103/PhysRevMaterials.7.095402.
[36] A. G. Jolley, R. Jayathilake, and E. D. Wachsman, Ionics **25**, 3531 (2019).
[37] M. Yashima and D. Ishimura, Chem. Phys. Lett. **378**, 395 (2003).
[38] M. Yashima, D. Ishimura, and K. Ohoyama, J. Am. Ceram. Soc. **88**, 2332 (2005).
[39] L. Klinkova, V. Nikolaichik, N. Barkovskii, and V. Fedotov, Russ. J. Inorg. Chem. **52**, 1822 (2007).
[40] P. Jacobs and D. Mac Donaill, Solid State Ion. **23**, 279 (1987).
[41] M. L. Tate, J. Hack, X. Kuang, G. J. McIntyre, R. L. Withers, M. R. Johnson, and I. R. Evans, J. Solid State Chem. **225**, 383 (2015).
[42] R. Chen, S.-L. Zhang, C.-J. Li, and C.-X. Li, J. Therm. Spray Technol. **30**, 196 (2021).
[43] T. B. Tran and A. Navrotsky, Chem. Mater. **24**, 4185 (2012).
[44] B. Schwaighofer, M. A. Gonzalez, M. Appel, M. M. Koza, and I. R. Evans, Chem. Mater. **35**, 1125 (2023).
[45] J. R. Peet, M. S. Chambers, A. Piovano, M. Johnson, and I. R. Evans, J. Mater. Chem. A **6**, 5129 (2018).
[46] P. Battle, T. Gibb, P. Lightfoot, and D. Munro, J. Solid State Chem. **83**, 31 (1989).
[47] P. Battle, C. Catlow, J. Heap, and L. Moroney, J. Solid State Chem. **63**, 8 (1986).
[48] P. Battle, C. Catlow, A. Chadwick, P. Cox, G. Greaves, and L. Moroney, J. Solid State Chem. **69**, 230 (1987).
[49] P. Battle, C. Catlow, J. Drennan, and A. Murray, J. Phys. C **16**, L561 (1983).
[50] P. Goel, M. Gupta, R. Mittal, S. Skinner, S. Mukhopadhyay, S. Rols, and S. Chaplot, J. Phys.: Condens. Matter **32**, 334002 (2020).
[51] P. Battle, C. Catlow, and L. Moroney, J. Solid State Chem. **67**, 42 (1987).
[52] G. Kresse and J. Furthmüller, Phys. Rev. B **54**, 11169 (1996).
[53] G. Kresse and D. Joubert, Phys. Rev. B **59**, 1758 (1999).
[54] J. P. Perdew, K. Burke, and M. Ernzerhof, Phys. Rev. Lett. **77**, 3865 (1996).
[55] H. J. Monkhorst and J. D. Pack, Phys. Rev. B **13**, 5188 (1976).
[56] B. Singh, M. K. Gupta, R. Mittal, M. Zbiri, S. Rols, S. J. Patwe, S. N. Achary, H. Schober, A. K. Tyagi, and S. L. Chaplot, J. Appl. Phys. **121**, 085106 (2017).
[57] R. J. Temkin, J. Non-Cryst. Solids **17**, 215 (1975).
[58] X. Wang, S. Tan, X.-Q. Yang, and E. Hu, Chin. Phys. B **29**, 028802 (2020).
[59] U. Dahlborg, W. Gudowski, and M. Davidovic, J. Phys.: Condens. Matter **1**, 6173 (1989).
[60] S. Kumar, M. K. Gupta, R. Mittal, N. H. Jalarvo, S. Mukhopadhyay, R. Shukla, S. N. Achary, A. I. Kolesnikov, A. K. Tyagi, and S. L. Chaplot, ACS Appl. Energy Mater. **5**, 14119 (2022).
[61] M. K. Gupta, P. Goel, R. Mittal, N. Choudhury, and S. L. Chaplot, Phys. Rev. B **85**, 184304 (2012).
[62] S. Kumar, M. K. Gupta, P. Goel, R. Mittal, O. Delaire, A. Thamizhavel, S. Rols, and S. L. Chaplot, Phys. Rev. Mater. **6**, 055403 (2022).
[63] Q. Ren, M. K. Gupta, M. Jin, J. Ding, J. Wu, Z. Chen, S. Lin, O. Fabelo, J. A. Rodríguez-Velamazán, M. Kofu, K. Nakajima, M. Wolf, F. Zhu, J. Wang, Z. Cheng, G. Wang, X. Tong, Y. Pei, O. Delaire, and J. Ma, Nat. Mater. **22**, 999 (2023).